$Pr_{0.5}Ca_{0.5}Mn_{0.97}Ga_{0.03}O_3$, a strongly strained system due to the coexistence of two orbital ordered phases at low temperature

C. Yaicle[a],*, F. Fauth[b], C. Martin[a], R. Retoux[a], Z. Jirak[c], M. Hervieu[a], B. Raveau[a], A. Maignan[a]

[a]Laboratoire CRISMAT, UMR 6508CNRS ENSICAEN, 6 bd Maréchal Juin, 14050 CAEN Cedex, France
[b]ESRF, BP 220, 6 Rue Jules Horowitz, F-38043 Grenoble, France
[c]Institute of Physics ACSR, Cukrovarnicka 10, 162 53 Prague 6, Czech Republic

Abstract

Combining low-temperature electron (ED) and synchrotron powder diffraction (SPD) techniques, we have precisely determined the phase-separated crystal structure of $Pr_{0.5}Ca_{0.5}Mn_{0.97}Ga_{0.03}O_3$. We demonstrate that the phase separation is associated with the onset of charge/orbital ordering at $\sim230\,K$ and that two ordered phases coexist at low temperature. In order to account for the significant anisotropic linewidth broadening observed in the SPD patterns, we had to include a specific strain model in the refinements. One of the phases, the most severely strained, is suggested to result from an imperfect charge ordering.
© 2005 Elsevier Inc. All rights reserved.

1. Introduction

The extremely rich magnetic and transport properties of the perovskite-based colossal magnetoresistive (CMR) manganites $Ln_{1-x}A_xMnO_3$ originate from a complex interaction between the lattice distortions and the spin, orbital and charge degrees of freedom [1,2]. In addition to these phenomena, the phase separation issue, and its role in the magnetic and transport properties, is still a matter of debate in the field of CMR manganites. First proposed as an inhomogeneous state at the microscopic scale, phase separation has also been evidenced to exist at a larger scale [3–10]. In most of the investigated systems, phase separation phenomena appeared to occur at the boundary between a charge-ordered antiferromagnetic (AFM) phase and a

charge disordered ferromagnetic state ($x \approx 0.3$–0.4 in the $Ln_{1-x}Ca_xMnO_3$ case). Hence, it was generally assumed that phase separation results from the coexistence of a ferromagnetic (FM) metal and an AFM insulator states. This is the case of the half-doped manganites $Ln_{0.5}Ca_{0.5}MnO_3$, where it is possible to favor metallic FM at the expense of insulating AFM by partially substituting Mn with a different cation. For instance, the substitution of Cr for Mn in $Ln_{0.5}Ca_{0.5}MnO_3$ induces ferromagnetism [11] but it is also susceptible to generate phase separation as shown for $Nd_{0.5}Ca_{0.5}Mn_{1-x}Cr_xO_3$ [12]. The study of half-doped manganites with non-magnetic cations substituted on the Mn lattice showed that this substitution weakens the charge/orbital ordering and the AFM character of the parent compound [13].

Recently, we focused on Ga-substituted manganites since they exhibit fascinating sharp magnetization steps as the magnetic field is increased [14]. The effect was

*Corresponding author. Fax: +33 2 31 56 73 50.
E-mail address: cedric.yaicle@ensicaen.fr (C. Yaicle).

interpreted in terms of a martensitic mechanism within a phase-separated picture [15]. Neutron powder diffraction (NPD) measurements in $Pr_{0.5}Ca_{0.5}Mn_{0.97}Ga_{0.03}O_3$ clearly evidenced a phase separation which consists of the coexistence of two antiferromagetic phases at low temperature. This study also showed that applying a magnetic field progressively induces magnetic (and structural) transitions in agreement with the steps observed in the $M(H)$ curves [16]. Without a magnetic field, each of the observed AFM-CE and AFM pseudo-CE states was described using a simple *Pnma*-type crystal structure, both structures differing, however, mainly in their unit cells and the MnO_6 distortions. Rietveld refinements of NPD data, including of course the magnetic contribution, lead to a 40/60 ratio for the AFM-CE "more distorted" and AFM-pseudo-CE "less distorted" phases, respectively. However, due to lack of angular resolution, the nuclear Bragg reflections could not be clearly distinguished from NPD data, neither could the thermal dependence of the phase segregation be established. The combined use of synchrotron X-ray powder diffraction (SPD) and electron diffraction (ED)/microscopy techniques appeared essential to describe more precisely the low-temperature state and thus to deepen the study of the phase separation occuring in $Pr_{0.5}Ca_{0.5}Mn_{0.97}Ga_{0.03}O_3$. It shows that this phenomenon, not only corresponds to the coexistence of two AFM types (CE and pseudo-CE) related to the presence of two differently distorted phases, but is also characterized by strong strains, which are suggested to originate from imperfect orbital ordering.

2. Experimental details

The sample of the present structural study is the same as previously used in the NPD measurements. Detailed synthesis conditions, by solid-state reaction at 1500 °C in air, are described in Ref. [16].

The ED studies were carried out with a JEOL 2010 CX microscope fitted with an eucentric goniometer ($\pm 60°$). The high-resolution electron microscopy (HREM) images were recorded at room temperature (RT) with a TOPCON 002B microscope (200 kV, $Cs = 0.4$ mm) and at 92 K with a JEOL 2011 FEG microscope. The three microscopes are equipped with an energy dispersive spectroscopy (EDS) analyzer. Pictures at 20 K were collected using a GATAN HCHDT 3010 liquid helium cooled sample holder used on the JEOL 2010 CX microscope.

SPD measurements were performed on the ID31 beamline of the European Synchrotron Radiation Facility (ESRF) in Grenoble in two stages. A first set of low-temperature patterns (10, 50, 100, 150 K and RT) was measured at a wavelength of 0.334971 Å using an

He-flow cryostat. A second set of data was registered at a similar wavelength (0.336349 Å) from 150 to 255 K in 15 K incremental steps using a nitrogen blower. Optimum transmission was achieved by enclosing the finely grounded sample in a 0.5 mm diameter borosilicate glass capillary and appropriate spinning (500 and 2000 rpm for the 1st and 2nd set, respectively) of the capillary in the beam ensured for a good powder averaging. Data were registered by scanning the 9-channels analyzer/scintillator detecting setup at a constant speed (0.5 and 2°/min) over 1–35° 2θ range. The 9 patterns were then properly merged and processed in order to achieve 0.002° effective step. Accurate instrumental resolution parameters were obtained by measuring a $Na_2Ca_3Al_2F_{14}$ (NAC) standard-type compound known to exhibit minimal sample broadening contribution. All the SPD data have been analyzed by the Rietveld method using the Fullprof package [17]. Profile parameters refined from the NAC sample were set and kept fixed for all refinements. In addition to the usual phase related parameters (scale factor, atom position and thermal motion parameters), anisotropic strain broadening parameters, according to Stephens' formalism [18], were allowed to vary.

3. Results

3.1. Room temperature study

The ED study coupled with EDS, performed on 35 crystallites, shows that the sample is single phase. All the crystallites exhibit the *Pnma*-type structure ($a_p\sqrt{2}$, $2a_p$, $a_p\sqrt{2}$; a_p refering to the cell parameter of the cubic perovskite) and are characterized by twinned domains, generated by the orthorhombic cell distortion. The EDS analyses lead to the average cationic composition $Pr_{0.50\pm0.03}Ca_{0.50\pm0.03}Mn_{0.97\pm0.01}Ga_{0.03\pm0.01}$ (0.03 and 0.01 correspond to the maximal experimental deviation with regard to the average value). The crystalline quality of the sample is illustrated by the HREM image in Fig. 1. It presents two twinned domains: [010] oriented in the left part of the image and [10$\bar{1}$] oriented in the right part. The high regularity of the image shows that there is no specific variation of the local contrast, which could be associated with the Ga for Mn substitution. The twin boundary (TB) appears planar in the thick part of the crystallite and parallel to (101) but in the top part of the image, the two domains overlap slightly. The domain size is commonly of a few hundred nanometers.

The RT SPD data are refined in the *Pnma* space group in agreement with the ED observations and the previous neutron diffraction study [16]. Structural
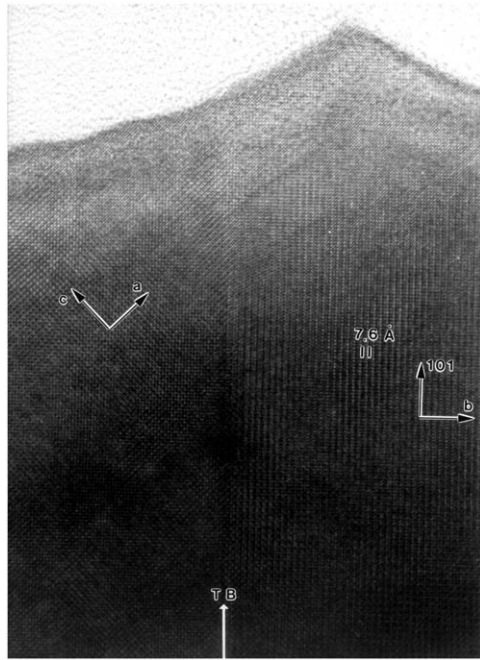
Fig. 1. $Pr_{0.5}Ca_{0.5}Mn_{0.97}Ga_{0.03}O_3$ room-temperature HREM image presenting two twinned domains oriented along [010] (left) and [10$\bar{1}$] (right) separated by a twin boundary labeled "TB". The distance "7.6 Å" corresponds to the b lattice parameter, in the $Pnma$ setting.

Table 1

Temperature	300 K	10 K	
		Phase I AFM pseudo-CE	Phase II AFM CE
Space group	*Pnma*	*Pnma*	
a (Å))	5.40223(1)	5.40880(8)	5.43245(4)
b(Å)	7.61670(2)	7.5725(1)	7.50130(3)
c(Å)	5.39334(1)	5.39887(7)	5.42758(4)
Volume (Å^3)	221.921(1)	221.128(6)	221.176(2)
Distortion	0.998	0.991	0.977
Pr, Ca site 4c			
x	0.02709(7)	0.03000(9)	0.0297(1)
y	0.25	0.25	0.25
z	−0.0049(2)	−0.0036(3)	−0.0051 (3)
B (Å^2)	0.589(6)	0.506(7)	0.37(1)
Mn, Ga site 4c			
x	0	0	0
y	0	0	0
z	0.5	0.5	0.5
B (Å^2)	0.292(9)	0.24(1)	0.20(2)
O(1) site 4c			
x	0.4912(5)	0.4934(7)	0.489(1)
y	0.25	0.25	0.25
z	0.0659(8)	0.0724(9)	0.070(1)
B (Å^2)	0.59(9)	0.8(1)	0.5(1)
O(2) site 8d			
x	0.2858(6)	0.2878(8)	0.287(1)
y	0.0345(3)	0.0376(4)	0.0384(5)
z	−0.2849(7)	−0.2850(9)	−0.281(1)
B (Å^2)	0.79(5)	0.77(6)	0.62(8)
Rwp (%)	3.76	1.94	3.26
χ^2	1.58	4.85	
Mn–O(1) (Å) × 2	1.9376(8)	1.933(1)	1.914(1)
Mn–O(2) (Å) × 2	1.941(3)	1.941(5)	1.938(6)
Mn–O(2) (Å) × 2	1.949(3)	1.963(4)	1.980(6)
Mn–O(1)–Mn (°)	158.67(3)	156.56(4)	156.96(5)
Mn–O(2)–Mn (°)	157.6(1)	156.4(2)	157.1(3)
Strain parameters			
S_400	0.249(3)	3.40(8)	0.347(9)
S_040	0.119(1)	3.76(8)	0.248(5)
S_004	0.172(5)	4.9(1)	0.65(2)
S_220	−0.124(5)	−5.7(1)	0.06(3)
S_202	1.14(1)	9.2(1)	1.47(4)
S_022	−0.093(6)	−7.4(2)	−0.28(3)
Lorentzian strain	0.113(2)	0	0.38(1)

parameters were first refined, leading to $R_{Bragg} = 5.54\%$ for 16 variable parameters (14 structural parameters, scale factor and zero shift). Then, whilst keeping fixed the profile parameters issued from the NAC measurements, 7 symmetry-dependent strain parameters were introduced in the refinement which account for the broadening of selected Bragg reflections. In this way the agreement factor is lowered to $R_{Bragg} = 3.76\%$, for the atomic coordinates listed in Table 1 and the patterns plotted in Fig. 2 (upper panel). The sample has pseudocubic metrics with a weak O′-type lattice distortion ($b/\sqrt{2} < c < a$), which can be suitably characterized with parameter $d = 0.998$ from the formula $500 = b * \sqrt{2}/(a + c)$. The selected interatomic distances and angles (Table 1) show that at RT the MnO_6 octahedra are slightly flattened along the b-axis with apical atomic distances of 1.938 Å, and two longer distances in the basal plane (1.941 and 1.949 Å). Although oxygen localization is known to be less precise using X-ray diffraction, we stress on the good agreement of the actual Mn–O distances with the previous values obtained by neutron diffraction [16].

The strain parameters used in our refinements follow the Stephens' formalism as fully described in Ref. [18]. Within this representation the strain broadening effects are considered as the manifestation of the distribution of lattice parameters. More precisely, the $1/d_{hkl}$ value (d_{hkl}

is the d-spacing between lattice planes of Miller indices hkl) stands as the mean value of a $1/d_{hkl}^2$-dependent distribution with variance:

$$\sigma^2(1/d_{hkl}^2) = \sum_{\substack{ij \\ \alpha_i = a,b,c,\alpha,\beta,\gamma}} \left\langle (\alpha_i - \langle \alpha_i \rangle)(\alpha_j - \langle \alpha_j \rangle) \right\rangle$$

$$\times \frac{\partial(1/d_{hkl}^2)}{\partial \alpha_i} \frac{\partial(1/d_{hkl}^2)}{\partial \alpha_j}$$

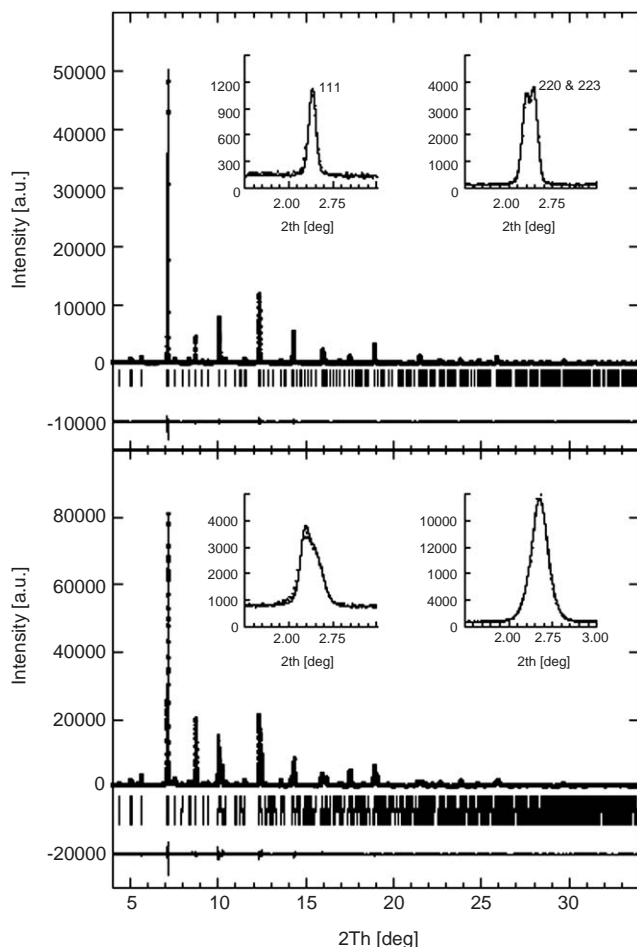$$= \sum_{\substack{HKL \\ H+K+L=4}} S_{HKL} h^H k^K l^L.$$

Fig. 2. $Pr_{0.5}Ca_{0.5}Mn_{0.97}Ga_{0.03}O_3$ RT (upper panel) and 10 K (lower panel) SPD patterns. From top to bottom: experimental (dots) and calculated (line), Bragg ticks (corresponding to the *Pnma* space groups) and difference plots. Few selected peaks are enlarged in inset to show the different broadening of the peaks (vs. 2θ and T).

The relation with the sample-dependent anisotropic line broadening is then expressed by

$$\Gamma^S(hkl) = \sqrt{\sigma^2(1/d_{hkl}^2)} \tan(\theta)/(1/d_{hkl}^2),$$

The Gaussian and Lorentzian part of the full-width at half-maximum (FWHM) of the *hkl* Bragg reflection are then expressed as

$$\Gamma_G = \sqrt{(\Gamma_G^I)^2 + (1-\xi)^2(\Gamma^S(hkl))^2}, \Gamma_L = \Gamma_L^I + \xi\Gamma^S(hkl),$$

where Γ_G^I, Γ_L^I are the instrumental (Gaussian and Lorentzian) FWHM as determined from the NAC measurements and ξ the Lorentzian-strain component parameter. As seen in Table 1, the Stephens strain parameter values refined from the RT pattern are very low and the reliability factors have been only slightly reduced by introducing anisotropic broadening parameters. In fact, the use of Stephens' formalism in this

particular case does not appear totally justified but as we will see below, it mainly serves for comparison purpose with the low-temperature data analysis. At this point, we add two remarks regarding the choice and signification of this microstructural model. Anisotropic line-width broadening can originate from several microstructural effects such as strain, size, twinning, dislocations, stacking faults, etc. (in fact, all the phenomena are most likely to interplay). Although a similar formalism for size effects broadening was developed by Stephens as well [18], the large extent of domains as observed from EM prompts us to apply the strain effect approach.

3.2. Low temperature state: synchrotron diffraction

The SPD pattern registered at 10 K immediately indicates, at first sight, a higher complexity as compared to the RT one (Figs. 2 and 3). Some Bragg reflections (e.g. 2 0 2 and 0 4 0) exhibit a considerably broadened linewidth, whereas the 0 2 2 and 2 2 0 ones remain constant. Moreover, residual intensity persists between peaks expected to be well resolved. Finally, the 1 1 1 reflection displays a structured profile (inset of Fig. 2 lower part) which unambiguously points towards a
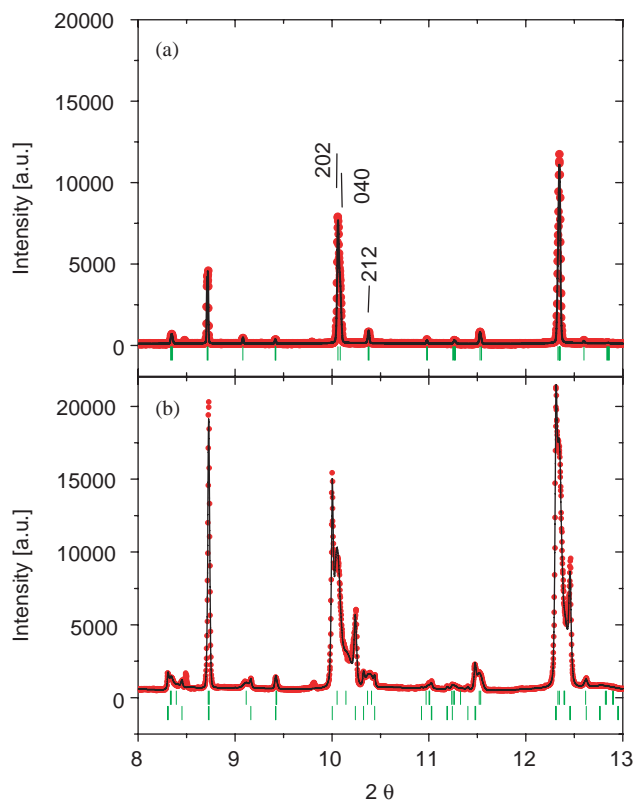

Fig. 3. Enlargement of experimental and calculated SPD patterns between 8° and 13° in 2θ: at RT (a) and at 10 K, refinements with two *Pnma* phases and strain parameters (b).

phase separation scenario as initially assumed based on previous NPD measurements [16]. Taking the NPD results as starting point, we carried out initial structure calculations based on the coexistence of two *Pnma* cells ($a_p\sqrt{2}$, $2a_p$, $a_p\sqrt{2}$) and the Stephens strain parameters were progressively introduced in the refinement of both *Pnma* phases. Results are given in Table 1 and calculated and observed profiles displayed in Figs. 2 and 3 (lower panels).

The obtained unit cell parameters and Mn–O distances show that both phases exhibit different distortions, in the *Pnma* symmetry. The phase labelled (I) is less distorted with $d = b * \sqrt{2}/(a + c) = 0.991$. The Mn–O interatomic distances are close to those of the RT phase, forming slightly flattened octahedra with comparable apical atomic distances of 1.933 Å, and a slightly more distorted basal plane (Mn–O_{eq} = 1.941 and 1.963 Å). The higher distorted phase (II), corresponding to $d = 0.977$, exhibits more flattened MnO_6 octahedra (Mn–O_{ap} = 1.914 Å) with larger distorted basal planes (Mn–$O_{eq} \approx 1.938$ and 1.980 Å). The difference between the unit cells, which develop together in a matrix starting from a unique *Pnma* space group when decreasing T, is necessarily responsible for the microstructural effects which lead to selected peak broadening. The corresponding strain parameters used in the calculations are refined to high values for the less distorted phase (I), which concerns the major part of the sample ($\approx 70\%$). On the other hand, the less distorted minority phase (II) has strain parameters similar to the RT ones. Once again, the ratio and the structural parameters of both phases are in good agreement with the previous NPD experiments, from which we can conclude that phases (I) and (II) are associated with AFM-pseudo-CE and AFM-CE-type magnetism, respectively [16]. Both the crystal and magnetic structures of phases (I) and (II) are reminiscent of $Pr_{0.6}Ca_{0.4}MnO_3$ and $Pr_{0.5}Ca_{0.5}MnO_3$, respectively [19], even if no evidence of charge ordering appears in the diffraction patterns of the Ga-substituted sample.

3.3. Low-temperature state: electron diffraction

The possibility of charge/orbital ordering (CO/OO) has been investigated by ED that is very sensitive to such phenomena. At 20 K it is found that, most of the crystallites exhibit the system of extra spots characteristic of CO/OO modulated structures [21,22], with $q = 0.5$ for roughly half of the modulated crystallites and $q = 0.5 - \varepsilon (\varepsilon_{max} \approx 0.05)$ for the remaining modulated crystallites. The same kind of behavior was observed at 92 and 20 K. The satellites are detectable below 230 K, which is in agreement with the beginning of the structural transition determined by the SPD study, even if no superstructure peaks are observed in the SPD patterns. Different modulation phenomena, added to

the twinned domains observed at RT (as shown in Fig. 4a), often make complex the low-temperature (LT) ED patterns, as illustrated by two typical examples in Fig. 4b and c. For numerous crystallites, the ED patterns are characterized by a splitting of the satellites, signature of an incommensurate modulation. The satellites are streaky and elongated along $a*$, the q values ranging between 0.45 and 0.5 (Fig. 4b). Nevertheless, for selected crystallites, the modulation can be commensurate ($q = 0.5$) with intense satellites (not shown). However, in Fig. 4b, the double-spots are not strictly aligned along $\vec{a}*$, involving that there exists a small component of the modulation vector along $\vec{c}*$. The second LT pattern shows two 90° oriented [010] domains with diffuse satellites along $a*$ and $a^{\perp}*$, respectively, and two 90° oriented [101] domains (Fig. 4c). This series of pictures illustrates the structural complexity of this compound at LT and thus the difficulty to simply describe this state.

Fig. 5a presents an HREM image recorded at 92 K, showing the coexistence of [101] (left part) and [010] domains (right part). The [010] domain exhibits a typical modulated contrast which corresponds to an average q value close to 0.48. The contrast is that of the *Pnma* subcell which consists of an array of bright spots, spaced along $\vec{a}$ and $\vec{c}$ by a distance close to 5.4 Å, and the modulated contrast along $\vec{a}$ results in the formation of double rows corresponding to the doubling of the a parameter observed at RT, in agreement with the "ideal" charge ordering schema [21,22]. Sometimes these double rows are separated by triple rows (denoted 2 and 3, respectively, in the image). This observation is in agreement with the incommensurate q value and shows that the modulation results from the local insertion of an additional row of bright spots. Moreover, such an image is commonly associated to diffuse satellites. The zone characterized by this disorder in the double rows arrangement is enlarged in Fig. 5b. Otherwise, locally close to the crystal edge, there exist areas in which only the contrast characteristic of the *Pnma* structure is observed, without any double nor triple periodicity whatever the focus value. Commonly, the modulation free areas, pointed by a black point in the lower part of Fig. 5a, are a few nanometers wide, never more. For the crystallites with $q = 0.5$ (not shown), the absence of additional rows implies a real doubling of the a parameters and the absence of discommensurations.

A very interesting information is provided by the LT contrasts. At low magnification, the low-temperature images show non-ideal contrasts, with variable intensity (darker and less darker zones), which could result from internal strains, between quite large domains (few tens of nm large). These effects are clearly evidenced in the dark field image recorded at LT (Fig. 6). At higher magnification, different states are observed, with or
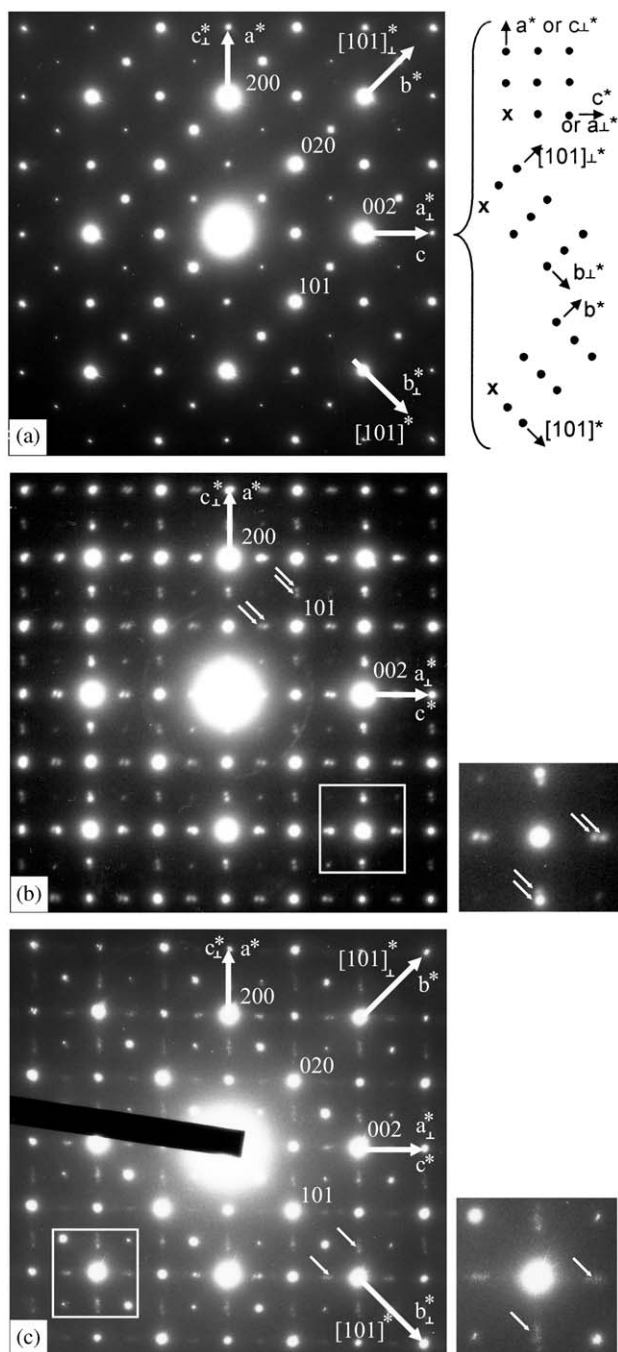
Fig. 5. HREM image recorded at 92 K. (a) The coexistence of [101] (left part) and [010] (right part) domains is observed. The [010] domain presents a typical contrast of the modulated structure. The contrast of the clear area indicated by the black point in the lower part is characteristic of a free modulation $Pnma$ structure. (b) Enlargement of the [010] domain shown in (a). The doubling of the a parameter "10.9 Å" is attributed to "ideal" CO. The presence of double rows separated by triple rows denoted "2" and "3" in the image is at the origin of the incommensurate character of the CO.

Fig. 4. $Pr_{0.5}Ca_{0.5}Mn_{0.97}Ga_{0.03}O_3$ ED patterns. For clarity, the indices representative of the a^*, c^* and b^*, [101]* direction have been written and the indices of the respective 90° oriented domains have been omitted. (a) RT diffraction pattern (left part) of a multidomain zone. This diffraction pattern results of the superimposition of different variants (two 90° oriented [10$\bar{1}$] patterns and two 90° oriented [010] patterns) schematized in the right part of the figure, each one corresponding to a domain of the crystal. (b) 92 K diffraction pattern of two 90° oriented [010] domains. Extra spots in incommensurate positions are pointed by white arrows ($q \approx 0.48$). (c) 92 K diffraction pattern recorded on a multidomain crystal (two 90° oriented [010] patterns with diffuse satellites along a^* and $a^{\perp*}$ and two 90° oriented [10$\bar{1}$] patterns). Compared to RT diffraction pattern (a), extra diffuse satellites are clearly evidenced (pointed by white arrows).
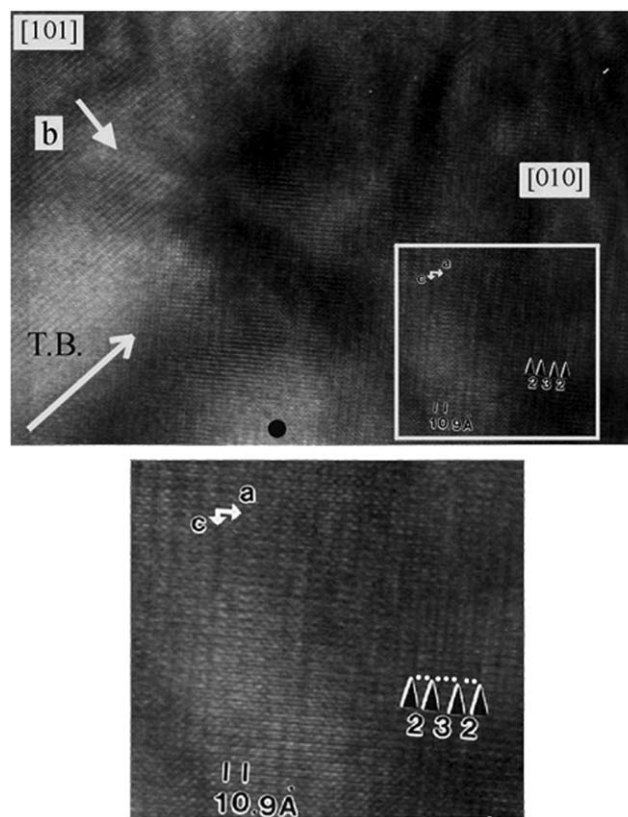
without disturbed contrasts, evidencing the spread of the strain in the matrix. To illustrate this point, the effect of temperature in a selected area is shown by the comparison between Figs. 7 (LT) and 1 (RT). At RT, this area exhibits an even contrast in the adjacent twinned domains with no strain effects, even at the level of the TB. At LT, the incommensurate modulation along $\vec{a}$ is clearly observed, the contrast is regular in both domains and no significant modification is detected at the level of the TB. On the opposite, as shown in Fig. 5, even at this nanometric scale, other parts exhibit a strongly disturbed contrast for area also with incommensurate modulation.

3.4. Thermal dependence of the crystal structures

The crystal structure evolution of $Pr_{0.5}Ca_{0.5}Mn_{0.97}$ $Ga_{0.03}O_3$ vs. T was analyzed from SPD data. Calculations were made using the two phases model up to 255 K. Based on the refined unit cell parameters as
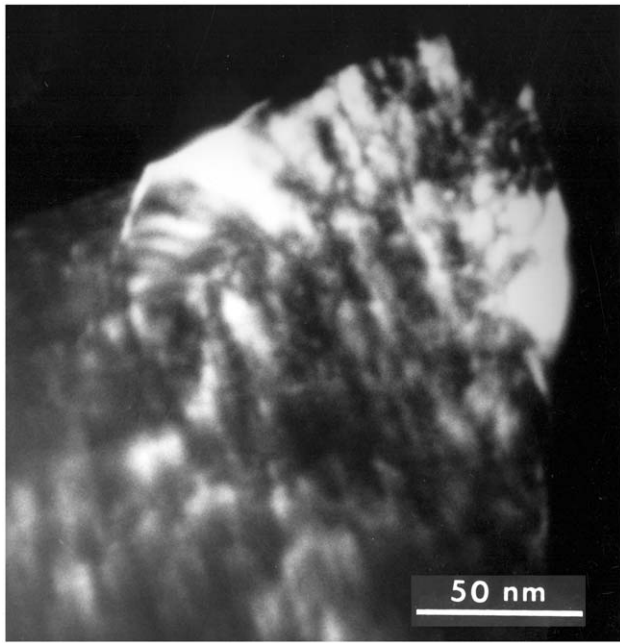
Fig. 6. 20 K dark field image of a multidomain crystal showing strong disturbed contrasts associated with strain phenomena in the grain.
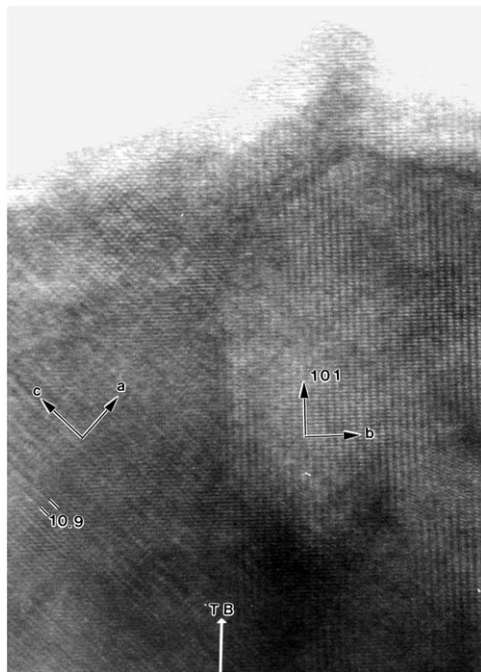

Fig. 7. 92 K HREM image of the area presented in Fig. 1. The incommensurate modulation induced by CO/OO is well established in the left part of the crystal (along a) but no significant perturbation of the contrast is detected, even at the level of the TB.
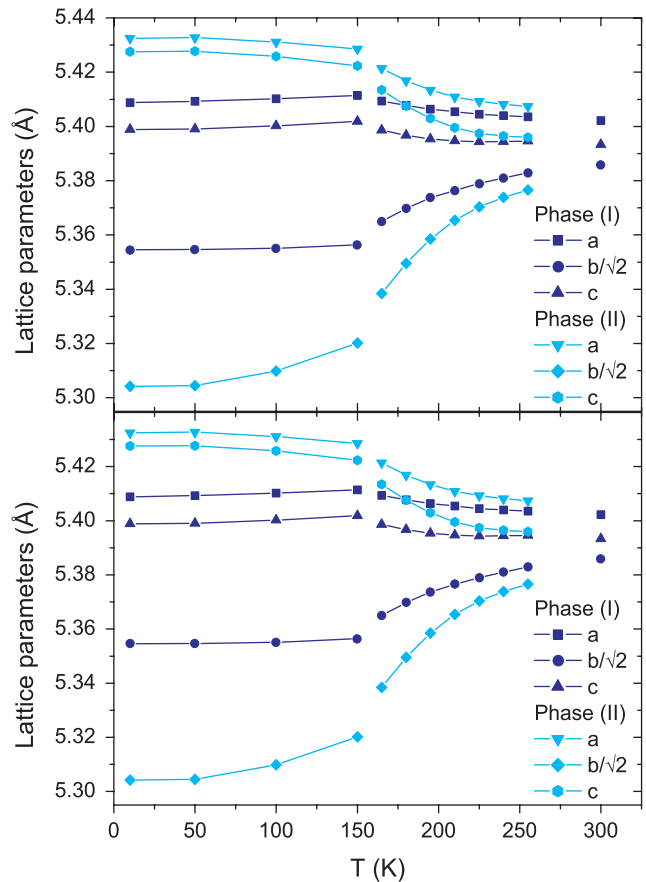

Fig. 8. (a) Lattice parameters evolution vs. T (from SPD data, increasing T). The lines are only a guide to the eyes and the missing lines (between 150 and 165 K) indicate the two sets of measurements (see experimental section). (b) Temperature dependence of the integral breath of few peaks (2 0 2, 0 4 0 and 2 1 2) for both phases (I and II).

displayed in Fig. 8a, we do not find evidence for a sharp transition from the two (LT) phases into a single one (RT). More importantly, the refined ratio between both phases (I/II) remains nearly constant ($\approx 70/30$) up to 255 K. However, when looking directly at the measured patterns, in particular the thermal dependence of the 1 1 1 Bragg reflection, we estimate the phase separation to occur around 225 K in warming, that is close to the T_{CO} determined by other techniques [16,23]. By decreasing T, the cell parameters of the minority phase II show a strong evolution towards a more distorted phase, but the strain parameters keep small values within the entire T range (Fig. 8b). In other words, in decreasing T, only a part of the matrix ($\approx 30\%$) tends to show a strong deformation, the transition begins to be visible below ≈ 250 K (because the metrics of the cells I and II become different enough to be observed by SPD). In contrast, the majority phase (I) displays a slighter lattice evolution but the strain parameters increase strongly below ≈ 225 K (Fig. 8b). Both the lattice and/ or strain parameters thermal evolutions occur in the temperarture range ~ 150–250 K, that is much higher than the AFM-CE and AFM-pseudo-CE magnetic transitions at $T_N \approx 90$ and 60 K, respectively [16]. This suggests a purely crystallographic origin of the phase

separation phenomena and the associated microstructural effects.

4. Discussion and conclusion

For each of the techniques used (NPD, ED and SPD), the characterization of a multiphase system like $Pr_{0.5}Ca_{0.5}Mn_{0.97}Ga_{0.03}O_3$ appears already tricky when considered individually. From NPD data [16], the coexistence of two distinct magnetic phases could be unambiguously established. Hence, data analysis was performed using a two crystallographic phases model although a clear separation of nuclear Bragg peaks was not observed. Moreover, the combined use of data collected under different experimental conditions (wavelength, angular resolution) appeared essential to get relevant structural information. The 60/40 ratio at 10 K for the AFM-pseudo-CE/AFM-CE phase as calculated in Ref. [16] is not so far from the 70/30 one obtained in the actual study considering the high correlations of the refined scaling factors and magnetic moments in the former case. This ratio would have been more accurate if calculated from NDP patterns collected in the paramagnetic phase (above 90 K). But the too close metrics of the coexisting phases at higher temperatures renders too uncertain a two phases refinement of data crucially missing of angular resolution.

ED is certainly the most valuable technique to directly probe charge/orbital ordering in powders. In $Pr_{0.5}Ca_{0.5}Mn_{0.97}Ga_{0.03}O_3$, the observation of several ordering variants (various scales, distribution of modulation parameter q) tends to confirm the multiphase nature of the low temperature state. However, a quantitative estimate of each phase is missing, unless performing a tedious analysis on enough specimens in order to get a satisfactory statistical ensemble. Here we stress that both the 'badly organized' CO/OO structure (as revealed by ED) and the strain broadening effects explain why no CO/OO superstructure peaks were observed in NPD and SPD measurements. The SPD experiment did not only evidence the crystallographic phase separation and determine its thermal dependence, it also revealed the highly strained character of (at least one of) the phases. The microstructural effects are most likely related to the associated phase separation and charge ordering processes assumed to occur ~230 K in $Pr_{0.5}Ca_{0.5}Mn_{0.97}Ga_{0.03}O_3$. The NPD measurements revealed at the lowest temperatures the coexistence of two AFM structures also observed in $Pr_{0.5}Ca_{0.5}MnO_3$ and $Pr_{0.6}Ca_{0.4}MnO_3$. Both compounds are known to exhibit the same kind of ordering, doubling of the unit cell along the a-axis, but with an incommensurate ($q = 0.5 - \varepsilon$) to commensurate ($q = 0.5$) structure when cooling down. Our ED pictures clearly evidence that various types of CO/OO structures, commensurate and incommensurate with varying modulation vectors, coexist in $Pr_{0.5}Ca_{0.5}Mn_{0.97}Ga_{0.03}O_3$ at a given temperature. Consequently, a distribution of the a-axis lattice parameter is expected. The two coexisting phases are as well characterized by specific thermal evolution of the b-axis parameter: the marked anomaly of b vs. T at $T \leqslant T_{CO}$ is of different strength for each phase.

In our SPD data refinements, we have applied the Stephens' formalism in order to take account of the significant broadening of selected Bragg peaks. The use of this phenomenological formalism was essential to complete the Rietveld refinements within a two phase model and obtain relevant results, as further validated by the good agreement with the previous NPD results. From a quantitative point of view, the refined strain parameter values do not really contribute to a better understanding of the microstructural effects, at least without the prior knowledge obtained from ED. Because all the 6 S_{hkl} strain parameters (4 of them significantly high) are refined to non-zero values, we cannot resume the effect to the distribution of only one of the cell parameters as was the case, e.g. in Ref. [20]. Moreover, the significant twinning effects observed in the material contribute to correlations of the strain parameters (typically, S040 and S202). In the present case, we mainly used the formalism to achieve satisfactory refinement and to determine relevant structural parameters of both coexisting phases. Nevertheless, the temperature dependence of the anisotropic broadening effect, as illustrated in Fig. 8b, is correlated to the nature of the CO/OO state and its onset. In this sense, the strain parameters can be seen as an order parameter to characterise the CO/OO. Thus it suggests that the phase I, which is the most highly strained, exhibits an incommensurate CO/OO ordering with varying modulation.

The present results can be compared to previous reports on an analogous compound $Pr_{0.5}Ca_{0.5}Mn_{0.95}Al_{0.05}O_3$, where disturbed ordered states were precisely described on the basis of ED observations [24]. In both cases (Al and Ga), the low-temperature states are similar: two crystallographic phases, two AFM (CE and pseudo-CE) structures with refined magnetic moments lower than the theoretical ones, short range CO/OO and coexistence of different q values. The comparison with other phase separated manganites with only Mn in the B-site of the perovskite is also interesting. A less pronounced broadening of peaks was also found in the synchrotron patterns of $La_{0.5}Ca_{0.5}MnO_3$, between 180 and 250 K that is between T_N and T_C [25]. It was interpreted as a single phase with a distribution of lattice parameters due to a static Jahn–Teller distortion leading to domains with different degrees of orbital ordering. More resemblance with the present Ga-substituted compound bears, however, the synchrotron data of $Pr_{0.7}Ca_{0.3}MnO_3$ [26], even if

the broadening effects are still smaller. The low-temperature state of this compound is described with two crystallographic cells, corresponding to FM and CE-AFM, associated with reverse orbital order and CO, respectively [26]. Note that for $Pr_{0.7}Ca_{0.3}MnO_3$, the phase separation (FM/AFM) is more obvious, since $q = 0.5$ for all the CO/OO part [27].

In conclusion, the onset of the structural phase separation at 230 K seems associated to the onset of charge/orbital ordering in $Pr_{0.5}Ca_{0.5}Mn_{0.97}Ga_{0.03}O_3$. The competition between different variants of charge ordering, when cooling down, but at 20 K as well, induces microstructural strains in both phases. The microstructural effects reported on both phases are probably responsible for the badly established magnetic order observed by NPD. We believe the highest strained phase (AFM pseudo CE) to have particular badly organized CO networks. We also stress that it is the same phase which collapses under an applied magnetic field, hence leading to the previously reported step-like magnetization effects. From an experimental point of view, the combination of electron, neutron and synchrotron powder diffraction techniques appeared essential to obtain a relevant unified picture of the low-temperature structure—crystal and magnetic—of $Pr_{0.5}Ca_{0.5}Mn_{0.97}Ga_{0.03}O_3$.

References

[1] Y. Tokura (Ed.), Colossal Magnetoresistance Oxides, Gordon & Breach, London, 1999.
[2] C.N.R. Rao, B. Raveau (Eds.), Colossal Magnetoresistance, Charge Ordering and Related Properties of Manganese Oxides, World Scientific, Singapore, 1998.
[3] S. Mori, C.H. Chen, S.-W. Cheong, Phys. Rev. Lett. 81 (1998) 3972.
[4] D.E. Cox, P.G. Radaelli, M. Marezio, S.W. Cheong, Phys. Rev. B 57 (1998) 3305.
[5] G. Allodi, R. De Renzi, F. Licci, M.W. Pieper, Phys. Rev. Lett. 81 (1998) 4736.
[6] M. Uhera, S. Mori, C.H. Chen, S.W. Cheong, Nature 399 (1999) 560.
[7] A. Moreo, S. Yunoki, E. Dagotto, Science 283 (1999) 2034.
[8] H.J. Lee, K.H. Kim, M.W. Kim, T.W. Noh, B.G. Kim, T.Y. Koo, S.-W. Cheong, Y.J. Wang, X. Wei, Phys. Rev. B 65 (2002) 115118.
[9] V. Podzorov, M.E. Gershenson, M. Uehara, S.-W. Cheong, Phys. Rev. B 64 (2001) 115113.
[10] T. Hotta, A.L. Malvezzi, E. Dagotto, Phys. Rev. B 62 (2000) 9432–9452.
[11] B. Raveau, A. Maignan, C. Martin, J. Solid State Chem. 130 (1997) 162.
[12] S. Mori, R. Shoji, N. Yamamoto, T. Asaka, Y. Matsui, A. Machida, Y. Moritomo, T. Katsufuji, Phys. Rev. B 67 (2003) 12403.
[13] S. Hébert, A. Maignan, C. Martin, B. Raveau, Solid State Commun. 121 (2002) 229.
[14] S. Hébert, V. Hardy, A. Maignan, R. Mahendiran, M. Hervieu, C. Martin, B. Raveau, J. Solid State Chem. 165 (2002) 6.
[15] V. Hardy, S. Majumdar, S.J. Crowe, M.R. Lees, D. McK. Paul, L. Hervé, A. Maignan, S. Hébert, C. Martin, C. Yaicle, M. Hervieu, B. Raveau, Phys. Rev. B 69 (2004) 020407(R).
[16] C. Yaicle, C. Martin, Z. Jirak, F. Fauth, G. André, E. Suard, A. Maignan, V. Hardy, R. Retoux, M. Hervieu, S. Hébert, B. Raveau, Ch. Simon, D. Saurel, A. Brûlet, F. Bourée, Phys. Rev. B 68 (2003) 224412.
[17] J. Rodriguez-Carvajal, Abstracts of Satellite Meeting on Powder Diffraction of XVth Congress International Union of Crystallography, Toulouse, 1990. p. 127.
[18] P.W. Stephens, J. Appl. Crystallogr. 32 (1999) 281.
[19] Z. Jirák, S. Krupicka, Z. Simsa, M. Dlouhá, S. Vratislav, J. Magn. Magn. Mater 53 (1985) 153.
[20] U. Staub, L. Soderholm, S. Skanthakumar, P. Pattison, K. Conder, Phys. Rev. B 57 (1998) 5535.
[21] F. Damay, Z. Jirak, M. Hervieu, C. Martin, A. Maignan, B. Raveau, G. André, F. Bourée, J. Magn. Magn. Mater. 190 (1998) 221.
[22] S. Mori, T. Katsufuji, N. Yamamoto, C.H. Chen, S.-W. Cheong, Phys. Rev. B 59 (1999) 13573–13576.
[23] A. Maignan, V. Hardy, C. Martin, S. Hébert, B. Raveau, J. Appl. Phys. 93 (2003) 7361.
[24] C. Martin, A. Maignan, F. Damay, M. Hervieu, B. Raveau, Z. Jirak, G. André, F. Bourée, J. Magn. Magn. Mater. 202 (1999) 11.
[25] P.G. Radaelli, D.E. Cox, M. Marezio, S.-W. Cheong, Phys. Rev. B 55 (1997) 3015.
[26] P.G. Radaelli, R.M. Ibberson, D.N. Argyriou, H. Casalta, K.H. Andersen, S.W. Cheong, J.F. Mitchell, Phys. Rev. B 63 (2001) 172419.
[27] M. Hervieu, A. Barnabé, C. Martin, A. Maignan, F. Damay, B. Raveau, Phys. Rev. B 60 (1999) R726.